Poly-superquadric model for DEM simulations of asymmetrically shaped particles

Siqiang Wang[1] · Shunying Ji[1]

Abstract

The superquadric function is employed to represent spherical and non-spherical particles. Although particles with different aspect ratios and surface blockiness can be described using the superquadric equation, the shapes of these particles are geometrically symmetric and further engineering applications are limited. In this work, a poly-superquadric element based on the superquadric function is developed. This model is composed of eight one-eighth superquadric elements and is used to represent superquadric elements, poly-ellipsoids, and asymmetrically shaped particles. To examine the validity of the poly-superquadric DEM model, the numerical results of a hemisphere impacting a plane are obtained and compared with the theoretical results. Then, the mass flow rates of particles of different shapes are investigated. The results show that the spheres have the fastest flow rate, and the flow rate of the pebble-shaped particles constructed by the poly-superquadric elements is faster than that of the cube-like particles. Moreover, the flow rate of superquadric and poly-superquadric elements decreases as the blockiness parameter increases. Geometrically asymmetric and elongated particles are rearranged to form interlocking and local clusters, which limit the relative motion between particles and reduce the flowability of non-spherical granular materials.

Keywords Discrete element method · Poly-superquadric model · Particle shape · Flow rate

1 Introduction

Granular materials are widespread in industrial production, and the discrete element method (DEM) is an effective method for studying the motion behavior of granular systems on the micro-scale [1–3]. Granular systems exhibited different phase transitions in a specific field, and the distribution of the contact force between elements on the micro-level might determine the flow transition of the granular systems on the macro–level [4]. As the particle roughness increased and the orifice diameter decreased, the spherical granular materials were more likely to transition from a flowing state to a non-flowing state [5]. Meanwhile, the flow behavior of the elements was transformed from mass flow to funnel flow by increasing the particle–wall friction [6]. Although most studies contribute to the motion behavior of spherical

particles, the flow characteristics of spherical particles are significantly different from those of non-spherical particles. The face-to-face contact between non-spherical particles facilitated energy dissipation caused by particle friction, which led to higher shear strength [7]. As the particle angularity increased, the discharge rate of non-spherical elements decreased and the residual quantity of particles increased [8]. More importantly, it was doubtful whether the numerical results obtained from spherical particles were applied to non-spherical particles [9]. Therefore, the non-spherical DEM model has always been a basic problem in numerical calculations [10, 11].

The single non-spherical DEM model has been widely established and applied to granular flow [12–14]. The ellipsoid element was constructed by the quadric equation and used to investigate the motion behaviors of ellipsoids within a rotating cylinder. Results indicated that the repose angle and coordination number of the ellipsoids increased as the aspect ratio deviated from 1 [15]. Cylindrical elements were used to simulate the hopper discharge of elongated particles, and the discharge rate decreased as the length of the cylinders increased [16]. The polyhedral

✉ Shunying Ji
jisy@dlut.edu.cn

1   State Key Laboratory of Structural Analysis for Industrial
     Equipment, Dalian University of Technology,
     Dalian 116024, China

elements were used to investigate the flow behavior of non-spherical particles in the hopper, and the discharge rate of polyhedral elements was lower than that of spherical elements [8, 17]. The dilated polyhedral elements were modeled by the Minkowski sum theory, and the increase in flow resistance and the formation of pile-ups at the bottom of the hopper were more pronounced for polyhedral elements than for dilated polyhedral elements [18]. Ellipsoids, cylinders, and cubes were constructed using the superquadric equation, and the particle shape determined the discharge rate of the monodisperse granular systems [19]. Moreover, novel construction methods for single non-spherical elements have been developed, including heart-shaped elements based on continue function representations [20], star-shaped elements based on harmonic functions [21], arbitrarily shaped elements based on level set functions [22], potential elements based on polynomial function [23], realistic granular samples based on random fields theory and Fourier shape descriptors [24], arbitrarily shaped elements based on the energy-conserving contact model [25, 26]. Although the novel construction theories can be used to describe arbitrarily shaped elements, their contact detections are complicated and the computational cost is high, which limits further large-scale engineering applications.

Recently, several elements have been combined to construct arbitrarily shaped particles and used to simulate the macroscopic properties of non-spherical granular materials [27]. The tetrahedral elements were constructed by the composed sphere method, and the results showed that locally ordered clusters were randomly distributed in the tetrahedral granular systems [28]. The sphero-cylinder elements were constructed through two hemispheres and a cylinder, and the orientations of sphero-cylinders were substantially perpendicular to the rotating axis to reduce energy dissipation [29]. A non-convex element was represented by glued convex particles, and the computational cost of DEM simulations was depended on the number of basic elements [30]. To reasonably describe the asymmetric geometry, the poly-ellipsoid was constructed through eight ellipsoids [31]. Each octant of the poly-ellipsoid was composed of one-eighth of an ellipsoid, and the numerical results of the axial compression of the poly-ellipsoids were closer to the experimental results than the ellipsoids [32]. Moreover, multi-superquadric elements were combined to represent an arbitrarily shaped particle, and the numerical results of tablets constructed with multi-superquadric elements were in good agreement with the experimental results [33]. Although the poly-superquadric elements were constructed by combining eight one-eighth superquadric elements, the hybrid Levenberg–Marquardt (LM) and Gilbert–Johnson–Keerthi (GJK) algorithms were complicated for determining the contact force between elements [34].

In this study, we introduce in detail a poly-superquadric model that can construct asymmetrically shaped particles. Moreover, eight bounding boxes are used for rough contact detection between basic elements, and the overlap between elements is calculated using the Newton iterative algorithm. Then, a hemisphere impacting a plane is simulated, and the numerical results are compared with the analytical results. Furthermore, the poly-superquadric model is used to simulate the dynamic accumulation and flow processes of the non-spherical particles. Finally, the influences of the particle shapes and hopper angles on the mass flow rate are investigated.

2 Non-spherical representation based on poly-superquadric equation

2.1 Description of the superquadric equation

The superquadric equation is an effective method for mathematically describing non-spherical particles, which is expressed as [35–37]

$$\left(\left| \frac{x}{a} \right|^{n_2} + \left| \frac{y}{b} \right|^{n_2} \right)^{n_1/n_2} + \left| \frac{z}{c} \right|^{n_1} - 1 = 0 \tag{1}$$

where a, b, and c are the semi-axial lengths of the superquadric element in the x, y, and z directions, respectively. n_1 and n_2 are the blockiness parameters, which are used to control different shapes and surface sharpness. The sphere and ellipsoid are constructed if $n_1 = n_2 = 2$, a cylinder-shaped element is constructed if $n_1 > n_2 = 2$ and a cube-shaped element is constructed if $n_1 = n_2 > 2$. Figure 1 shows differently shaped particles constructed by changing the five parameters of the superquadric equation.

2.2 Description of the poly-superquadric equation

A poly-superquadric particle is composed of eight one-eighth superquadric elements, and Eq. (1) is used to determine each basic superquadric element. The function of a poly-superquadric element is expressed as [34]

$$\left(\left| \frac{x}{a_k} \right|^{n_{2k}} + \left| \frac{y}{b_k} \right|^{n_{2k}} \right)^{n_{1k}/n_{2k}} + \left| \frac{z}{c_k} \right|^{n_{1k}} - 1 = 0 \quad (k = 1, 2, 3, \ldots, 7, 8) \tag{2}$$

where a_k, b_k, c_k, n_{1k}, and n_{2k} are the function parameters of the k th superquadric element. The value of k is equal to 8, and a poly-superquadric element is modeled by 40 function parameters. Meanwhile, the governing equation for the smooth and continuous particle surface can be expressed as

Fig. 1 Different shapes of particles represented by the superquadric equation

$$a_1 = a_4 = a_5 = a_8 = r_x^+, (x > 0) \tag{3}$$

$$a_2 = a_3 = a_6 = a_7 = r_x^-, (x < 0) \tag{4}$$
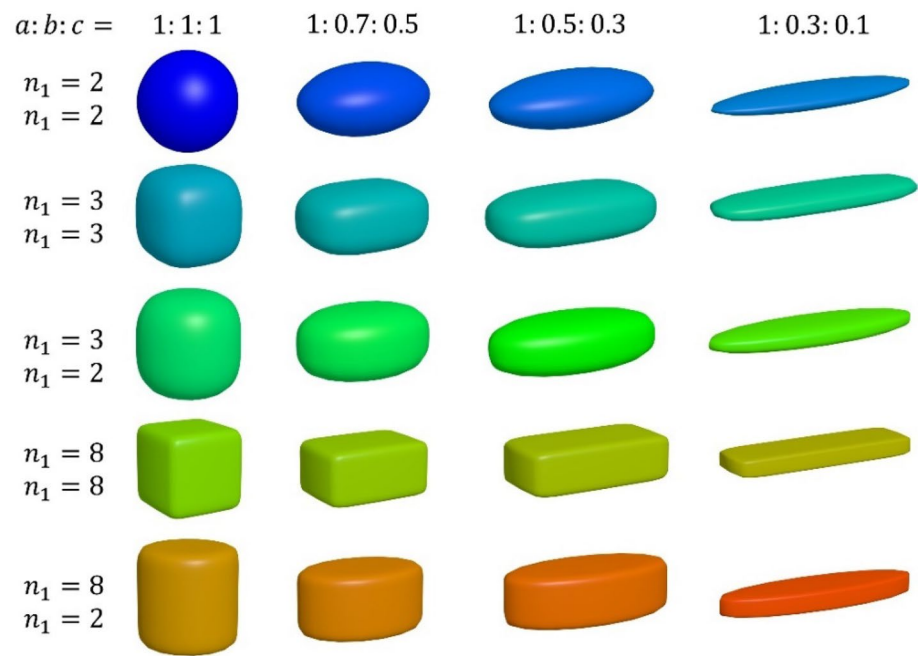
$$b_1 = b_2 = b_5 = b_6 = r_y^+, (y > 0) \tag{5}$$

$$b_3 = b_4 = b_7 = b_8 = r_y^-, (y < 0) \tag{6}$$

$$c_1 = c_2 = c_3 = c_4 = r_z^+, (z > 0) \tag{7}$$

$$c_5 = c_6 = c_7 = c_8 = r_z^-, (z < 0) \tag{8}$$

$$n_{11} = n_{12} = n_{13} = n_{14} = n_{15} = n_{16} = n_{17} = n_{18} = n_1^* \tag{9}$$

$$n_{21} = n_{22} = n_{23} = n_{24} = n_{25} = n_{26} = n_{27} = n_{28} = n_2^* \tag{10}$$

where $r_x^+, r_x^-, r_y^+, r_y^- r_z^+, r_z^-$ are the lengths of the poly-superquadric element in the positive and negative directions of the x, y, and z axis, respectively. n_1^* and n_2^* are the shape parameters of the poly-superquadric element. Therefore, only 8 parameters are needed to determine the shape of a poly-superquadric element. Figure 2 shows a poly-superquadric
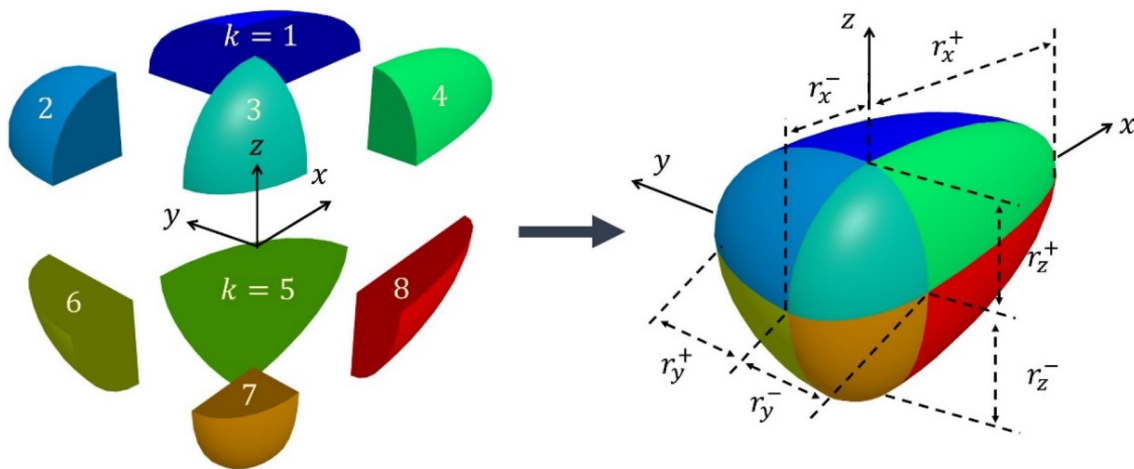
Fig. 2 A poly-superquadric element composed of eight one-eighth superquadric elements

element composed of eight one-eighth superquadric elements. Moreover, poly-superquadric elements of different shapes are obtained by changing eight shape parameters, as shown in Fig. 3. Poly-ellipsoid elements are obtained if $n_1^* = n_2^* = 2$ [32], and superquadric elements of different shapes are obtained if $r_x^+ = r_x^-$, $r_y^+ = r_y^-$, and $r_z^+ = r_z^-$.
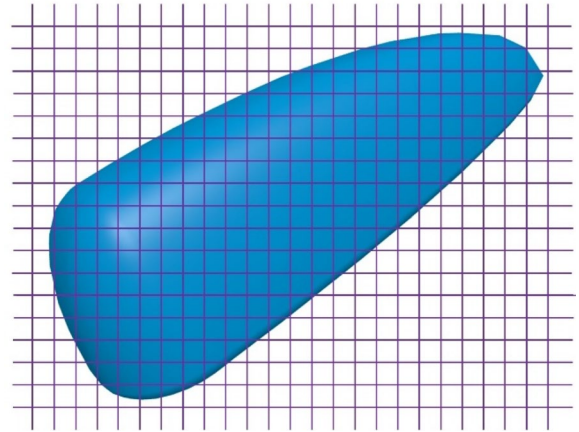
3 Search method of poly-superquadric elements

The numerical simulation of the poly-superquadric DEM model is complicated and consists of three parts: calculation of mass and moment of inertia, contact algorithm between particles, and update of particle position. These parts are described in the following chapters.
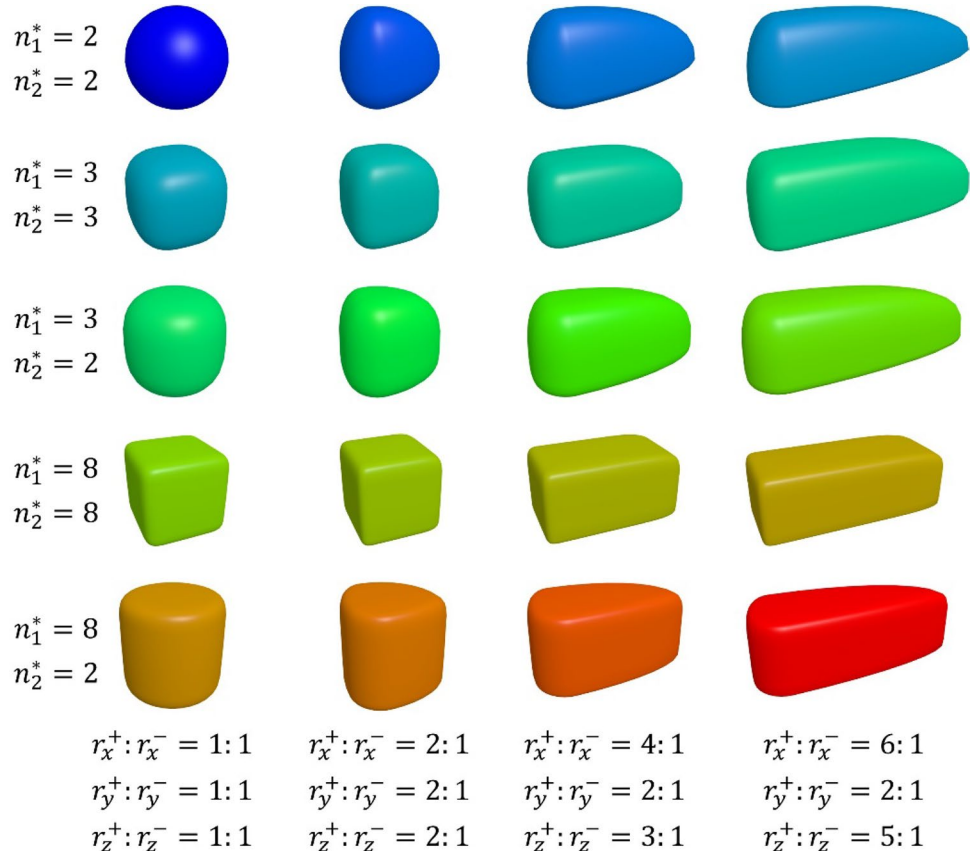
3.1 Calculation of mass and moment of inertia

The mass, mass center, and moment of inertia of a poly-superquadric element can be obtained by weighting the relevant parameters of eight one-eighth superquadric elements, and more detailed calculations can be found in Ref. [34]. In this paper, the background grid is used to simplify the calculation of the real information of the elements, as shown in Fig. 4.

The size of each cube grid is one-eighth of the minimum of the three semi-axis lengths of the eight superquadric elements. Subsequently, each effective grid is obtained through the positional relationship between the grid centroid and the element, and the mass of all effective grids is accumulated to represent the real information of the elements. Therefore, the mass of a poly-superquadric element can be expressed as

Fig. 4 Background grid method for calculating the mass and moment of inertia of poly-superquadric elements

Fig. 3 Different shapes of particles represented by the poly-superquadric equation

$$n_1^* = 2$$
$$n_2^* = 2$$

$$n_1^* = 3$$
$$n_2^* = 3$$

$$n_1^* = 3$$
$$n_2^* = 2$$

$$n_1^* = 8$$
$$n_2^* = 8$$

$$n_1^* = 8$$
$$n_2^* = 2$$

$r_x^+ : r_x^- = 1 : 1$	$r_x^+ : r_x^- = 2 : 1$	$r_x^+ : r_x^- = 4 : 1$	$r_x^+ : r_x^- = 6 : 1$
$r_y^+ : r_y^- = 1 : 1$	$r_y^+ : r_y^- = 2 : 1$	$r_y^+ : r_y^- = 2 : 1$	$r_y^+ : r_y^- = 2 : 1$
$r_z^+ : r_z^- = 1 : 1$	$r_z^+ : r_z^- = 2 : 1$	$r_z^+ : r_z^- = 3 : 1$	$r_z^+ : r_z^- = 5 : 1$

$$M_s = \sum_{nz=1}^{N_z} \sum_{ny=1}^{N_y} \sum_{nx=1}^{N_x} \rho l_{nx} l_{ny} l_{nz} \qquad (11)$$

where M_s and ρ are mass and particle density, respectively. l_n is the length of the grid, and N is the total number of effective grids. The subscripts x, y, and z indicate the components in the x-, y-, z-directions, respectively. The element centroid is obtained by

$$C_x = \frac{1}{M_s} \sum_{nz=1}^{N_z} \sum_{ny=1}^{N_y} \sum_{nx=1}^{N_x} \rho l_{nx} l_{ny} l_{nz} x_g \qquad (12)$$

$$C_y = \frac{1}{M_s} \sum_{nz=1}^{N_z} \sum_{ny=1}^{N_y} \sum_{nx=1}^{N_x} \rho l_{nx} l_{ny} l_{nz} y_g \qquad (13)$$

$$C_z = \frac{1}{M_s} \sum_{nz=1}^{N_z} \sum_{ny=1}^{N_y} \sum_{nx=1}^{N_x} \rho l_{nx} l_{ny} l_{nz} z_g \qquad (14)$$

where C_x, C_y, and C_z are the centroid coordinates of the element. x_g, y_g, and z_g are the center coordinates of the grid. In addition, the moments of inertia of the element are obtained by

$$I_{xx} = \sum_{nz=1}^{N_z} \sum_{ny=1}^{N_y} \sum_{nx=1}^{N_x} \rho l_{nx} l_{ny} l_{nz} \left[\left(y_g - C_y\right)^2 + \left(z_g - C_z\right)^2 \right] \qquad (15)$$

$$I_{yy} = \sum_{nz=1}^{N_z} \sum_{ny=1}^{N_y} \sum_{nx=1}^{N_x} \rho l_{nx} l_{ny} l_{nz} \left[\left(x_g - C_x\right)^2 + \left(z_g - C_z\right)^2 \right] \qquad (16)$$

$$I_{zz} = \sum_{nz=1}^{N_z} \sum_{ny=1}^{N_y} \sum_{nx=1}^{N_x} \rho l_{nx} l_{ny} l_{nz} \left[\left(x_g - C_x\right)^2 + \left(y_g - C_y\right)^2 \right]. \qquad (17)$$

3.2 Contact algorithm between particles

A poly-superquadric element consists of eight one-eighth superquadric elements, and the contact algorithm of the poly-superquadric elements is transformed into the contact algorithm of the superquadric elements. Subsequently, the quadrant position of the contact point in the local coordinate system is used to determine whether the point is on the surface of the one-eighth superquadric element. Moreover, the search between elements is not performed for two basic superquadric elements belonging to the same poly-superquadric particle.

Generally, bounding spheres and orientated bounding boxes are used to reduce the number of contact pairs between elements and improve the computational efficiency of DEM simulations, as shown in Fig. 5. The search of the bounding sphere is performed as the first rough detection between poly-superquadric elements. If the distance between the centers of neighboring elements is less than the sum of the bounding radii, the two elements may be in contact. Subsequently, the oriented bounding box is used for the second rough detection between poly-superquadric elements. A poly-superquadric element has eight sub-bounding boxes, and a basic superquadric element is surrounded by one sub-bounding box. If the sum of the distances of the bounding boxes projected on the separating axis is less than the projection distance between the centroids of the two superquadric elements, the two elements are not in contact. More detailed information about bounding box calculations can be found in Ref. [38].

Moreover, the accurate contact detection between superquadric elements has been well established, including the common normal approach [39], geometric potential concept [40], and midway point method [41]. Here, the overlap between two superquadric elements i and j is calculated by the midway point method. The nonlinear equations for calculating the midway point $\left(X_0\right)$ between the elements are expressed as [42]

Fig. 5 Rough contact detection between poly-superquadric elements: **a** a bounding sphere and **b** an oriented bounding box

(a)

(b)
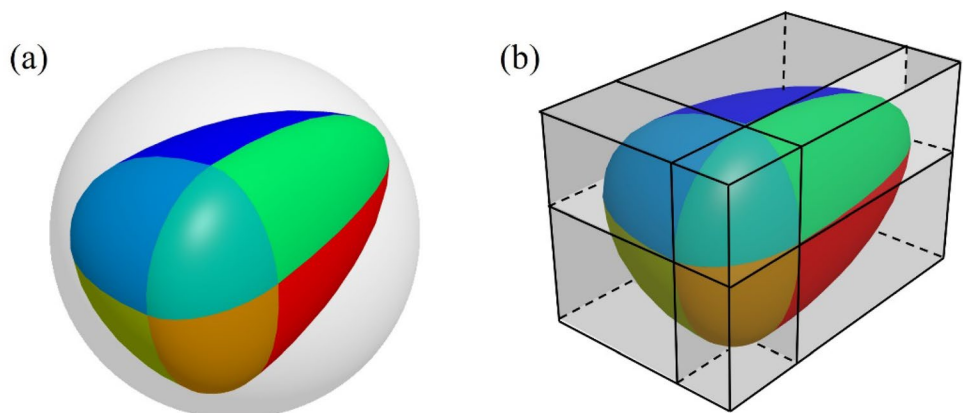
$$\begin{cases} \nabla F_i(\boldsymbol{X}) + \lambda^2 \nabla F_j(\boldsymbol{X}) = 0 \\ F_i(\boldsymbol{X}) - F_j(\boldsymbol{X}) = 0 \end{cases} \tag{18}$$

where $\boldsymbol{X} = (x, y, z)^{\mathrm{T}}$ and λ is a multiplier. F_i and F_j are the functional equations of elements i and j, respectively. The Newton iteration algorithm can be used to solve nonlinear equations, expressed as [41]

$$\begin{pmatrix} \nabla^2 F_i(\boldsymbol{X}) + \lambda^2 \nabla F_j(\boldsymbol{X}) & 2\lambda \nabla F_j(\boldsymbol{X}) \\ \nabla F_i(\boldsymbol{X}) - \nabla F_j(\boldsymbol{X}) & 0 \end{pmatrix} \begin{pmatrix} \mathrm{d}\boldsymbol{X} \\ \mathrm{d}\lambda \end{pmatrix}$$
$$= -\begin{pmatrix} \nabla F_i(\boldsymbol{X}) + \lambda^2 \nabla F_j(\boldsymbol{X}) \\ F_i(\boldsymbol{X}) - F_j(\boldsymbol{X}) \end{pmatrix} \tag{19}$$

where $\boldsymbol{X}^{(k+1)} = \boldsymbol{X}^{(k)} + \mathrm{d}\boldsymbol{X}$ and $\lambda^{(k+1)} = \lambda^{(k)} + \mathrm{d}\lambda$. If the midway point $\boldsymbol{X}_0$ satisfies $F_i(\boldsymbol{X}_0) < 0$ and $F_j(\boldsymbol{X}_0) < 0$, element i may be in contact with element j, as shown in Fig. 6. Subsequently, the point $\boldsymbol{X}_0$ in the global coordinate system is transformed to the points $\boldsymbol{X}_{0,i}^l$ and $\boldsymbol{X}_{0,j}^l$ of elements i and j in the local coordinate system, respectively. If the quadrants of the points $\boldsymbol{X}_{0,i}^l$ and $\boldsymbol{X}_{0,j}^l$ are the same as the quadrants of the one-eighth superquadric elements i and j, the midway point $\boldsymbol{X}_0$ is the contact point between the elements i and j. The normal direction ($\boldsymbol{n}$) is obtained by $\boldsymbol{n} = \nabla F_i(\boldsymbol{X}_0)/\nabla F_i(\boldsymbol{X}_0)$ or $\boldsymbol{n} = -\nabla F_j(\boldsymbol{X}_0)/\nabla F_j(\boldsymbol{X}_0)$. Finally, the surface points $\boldsymbol{X}_i$ and $\boldsymbol{X}_j$ of elements i and j are expressed as $\boldsymbol{X}_i = \boldsymbol{X}_0 + \gamma\boldsymbol{n}$ and $\boldsymbol{X}_j = \boldsymbol{X}_0 + \beta\boldsymbol{n}$, respectively. The parameters γ and β are obtained by Newton's iterative algorithm: $\gamma^{(k+1)} = \gamma^{(k)} - F_i(\boldsymbol{X}_i^{(k)})/(\nabla F_i(\boldsymbol{X}_i^{(k)})\boldsymbol{n})$ and $\beta^{(k+1)} = \beta^{(k)} - F_j(\boldsymbol{X}_j^{(k)})/(\nabla F_j(\boldsymbol{X}_j^{(k)})\boldsymbol{n})$. Therefore, the normal overlap between elements can be obtained by $\boldsymbol{\delta}_n = \boldsymbol{X}_i - \boldsymbol{X}_j$.
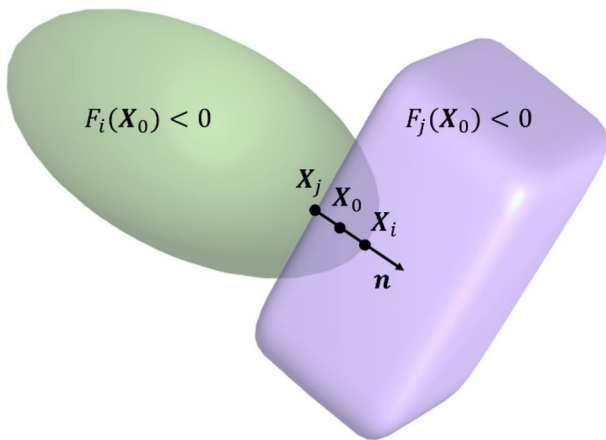

Fig. 6 Accurate contact detection between superquadric elements

3.3 Update of particle position

According to the DEM, a poly-superquadric element has translational and rotational motions, which is governed by Newton's second law of motion:

$$m_i \frac{\mathrm{d}\boldsymbol{v}_i}{\mathrm{d}t} = \sum_{j=1}^{N_s} (\boldsymbol{F}_{n,ij} + \boldsymbol{F}_{t,ij}) + m_i\boldsymbol{g} \tag{20}$$

$$\boldsymbol{I}_i \frac{\mathrm{d}\boldsymbol{\omega}_i}{\mathrm{d}t} = \sum_{j=1}^{N_s} (\boldsymbol{M}_{n,ij} + \boldsymbol{M}_{t,ij} + \boldsymbol{M}_{r,ij}) \tag{21}$$

where m_i and $\boldsymbol{I}_i$ are the mass and moment of inertia of the poly-superquadric element i, respectively. $\boldsymbol{v}_i$ and $\boldsymbol{\omega}_i$ are the translation and rotation speeds of the poly-superquadric element i, respectively. $\boldsymbol{F}_{n,ij}$ and $\boldsymbol{F}_{t,ij}$ are the normal and tangential forces acting on the poly-superquadric element, respectively. $\boldsymbol{M}_{n,ij}$ and $\boldsymbol{M}_{t,ij}$ are the normal and tangential moments caused by the forces $\boldsymbol{F}_{n,ij}$ and $\boldsymbol{F}_{t,ij}$, respectively, when the normal force does not pass through the centroid of the poly-superquadric element. $\boldsymbol{M}_{r,ij}$ is the rolling friction torque. N_s is the total number of elements acting on the poly-superquadric element i. In addition, the nonlinear contact model of spherical particles has been well applied to calculate the force between non-spherical particles [43–45]. The total normal force ($\boldsymbol{F}_{n,ij}$) consists of the normal elastic force ($\boldsymbol{F}_{n,ij}^e$) and the normal damping force ($\boldsymbol{F}_{n,ij}^d$). The total tangential force ($\boldsymbol{F}_{t,ij}$) consists of the tangential elastic force ($\boldsymbol{F}_{t,ij}^e$) and the tangential damping force ($\boldsymbol{F}_{t,ij}^d$), as shown in Table 1. Meanwhile, R_i and R_j are substituted by the radii of the volume equivalent spheres of particles i and j, respectively.

For poly-superquadric elements, the quaternion method is used to describe the orientation of non-spherical elements. The transformation matrix $\boldsymbol{R}$ represented by the quaternion $\boldsymbol{Q}(q_0, q_1, q_2, q_3)$ can be expressed as

$$\boldsymbol{R} = \begin{bmatrix} q_0^2 + q_1^2 - q_2^2 - q_3^2 & 2(q_1q_2 + q_0q_3) & 2(q_1q_3 - q_0q_2) \\ 2(q_1q_2 - q_0q_3) & q_0^2 - q_1^2 + q_2^2 - q_3^2 & 2(q_2q_3 + q_0q_1) \\ 2(q_1q_3 + q_0q_2) & 2(q_2q_3 - q_0q_1) & q_0^2 - q_1^2 - q_2^2 + q_3^2 \end{bmatrix} \tag{22}$$

Here, the transition relationship between the local coordinate system ($\boldsymbol{v}^l$) and the global coordinate system ($\boldsymbol{v}^g$) is expressed as

$$\boldsymbol{v}^l = \boldsymbol{R}\boldsymbol{v}^g \tag{23}$$

The matrix $\boldsymbol{R}$ satisfies $\boldsymbol{R}^T = \boldsymbol{R}^{-1}$. The rotational motions of the element (i) are expressed as

$$I_{xx,i}\frac{\mathrm{d}\omega_{x,i}^l}{\mathrm{d}t} + (I_{zz,i} - I_{yy,i})\omega_{y,i}^l\omega_{z,i}^l = M_{x,ij}^l \tag{24}$$

$$I_{yy,i}\frac{d\omega_{y,i}^l}{dt} + \left(I_{xx,i} - I_{zz,i}\right)\omega_{z,i}^l\omega_{x,i}^l = M_{y,ij}^l \tag{25}$$

$$I_{zz,i}\frac{d\omega_{z,i}^l}{dt} + \left(I_{yy,i} - I_{xx,i}\right)\omega_{x,i}^l\omega_{y,i}^l = M_{z,ij}^l \tag{26}$$

where the superscript l denotes the component in the local coordinate system, and the subscripts x, y, and z represent the components in the x, y, and z directions, respectively. The detailed calculation of quaternion can be found in Refs. [46–48]. It is worth noting that the coordinate origin and centroid of the poly-superquadric element are different. At the initial moment, the positional relationship between the origin coordinate $\left(O_0\right)$ and mass center $\left(O_c\right)$ should be determined, as shown in Fig. 7. $\boldsymbol{R}_0$ is the transformation matrix of a poly-superquadric element, which is used to represent the orientation of the poly-superquadric element. The vector $\boldsymbol{v}_c^l$ directs from point O_c to point O_0, and remains unchanged in the DEM simulation. Furthermore, the centroid position $\left(\boldsymbol{X}_c\right)$ of the poly-superquadric element in the global coordinate system is calculated at each DEM step. The origin coordinate $\left(\boldsymbol{X}_0\right)$ is obtained by $\boldsymbol{X}_0 = \boldsymbol{X}_c + \boldsymbol{R}_0^T\boldsymbol{v}_c^l$ and used to update the position of the basic superquadric elements.

4 DEM simulations of poly-superquadric elements

To examine the validity of the poly-superquadric model, the numerical results of a hemisphere impacting a plane are compared with the theoretical results. Then, the influences of particle shape on the flow characteristics of the granular materials are investigated.
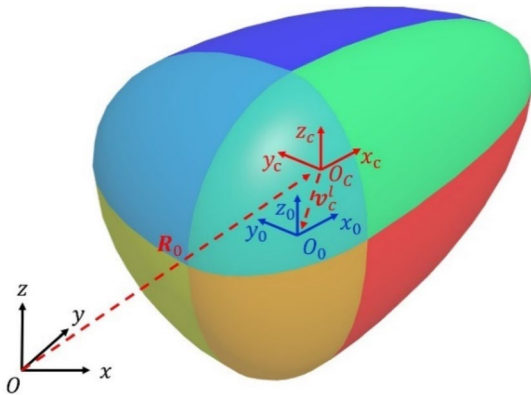
Fig. 7 Relationship between the mass center and origin coordinate of the poly-superquadric element

4.1 Verification of single-particle collisions

To verify the poly-superquadric DEM model, a hemisphere impacting a plane is simulated. An approximate hemisphere is represented by a poly-superquadric element, as shown in Fig. 8a. A poly-superquadric element has the parameters of $r_x^+ = r_y^+ = r_y^- = r_z^+ = r_z^- = r_0 = 6$ mm, $r_x^- = 0.01$ mm, and $n_1^* = n_2^* = 2$. Moreover, the distance $\left(c_0\right)$ between the mass center $\left(O_c\right)$ and the center $\left(O_0\right)$ of the sphere is expressed as $c_0 = 3r_0/8$, and the density of the element is 2500 kg/m³. The mass (m) and the y-axis moment $\left(I_{yy}\right)$ of inertia of the actual hemisphere are 1.131×10^{-3}kg and $1.056 \times 10^{-8}\left(\text{kg} \cdot \text{m}^2\right)$, respectively, and the mass and the y-axis moment of inertia of the approximate hemisphere are 1.131×10^{-3}kg and $1.056 \times 10^{-8}\left(\text{kg} \cdot \text{m}^2\right)$, respectively. Besides, gravity and particle–wall friction are not considered in the impact process. The rebound angular speed $\left(w_y^+\right)$ and translational speed $\left(v_z^+\right)$ are obtained by [49]

$$w_y^+ = -mv_z^-(1 + \varepsilon)c_0\cos\left(\varphi_0\right)/\left(I_{yy} + mc_0^2\cos^2\left(\varphi_0\right)\right) \tag{27}$$

$$v_z^+ = -w_y^+c_0\cos\left(\varphi_0\right) - \varepsilon v_z^- \tag{28}$$

where φ_0 is the angle between the hemispherical plane and the line connecting the center of the sphere and the contact point. v_z^- is the initial impact speed, which is equal to -1 m/s. ε is the coefficient of restitution, which is equal to 0.85. The main calculation parameters are listed in Table 2.

The changes of the dimensionless rebound angular speed $\left(r_0w_y^+/v_z^-\right)$ and rebound speed $\left(v_z^+/v_z^-\right)$ of the hemisphere with the impact time are shown in Fig. 8b. Here, the impact angle $\varphi_0 = 30^{\circ}$. Meanwhile, the dimensionless rebound angular speed and rebound speed of different impact angles are compared with the theoretical results, as shown in Fig. 8c, d. Although there is a slight difference between the hemisphere constructed by the poly-superquadric DEM model and the real hemisphere, the DEM results are in good agreement with the analytical results [49], which indicates that the aforementioned poly-superquadric DEM model is suitable for simulating the motion behavior of non-spherical particles.

5 Packing and flow process of the granular materials

The particle shape significantly affects the flow characteristics of the particles. Firstly, the formation of spherical and non-spherical granular beds is simulated by the superquadric and poly-superquadric models. A sphere constructed by the superquadric model has parameters of $a : b : c = 1 : 1 : 1$ and $n_1 = n_2 = 2$. A pebble-like particle constructed by the poly-superquadric model has parameters of $r_x^+ : r_x^- = 0.7$,
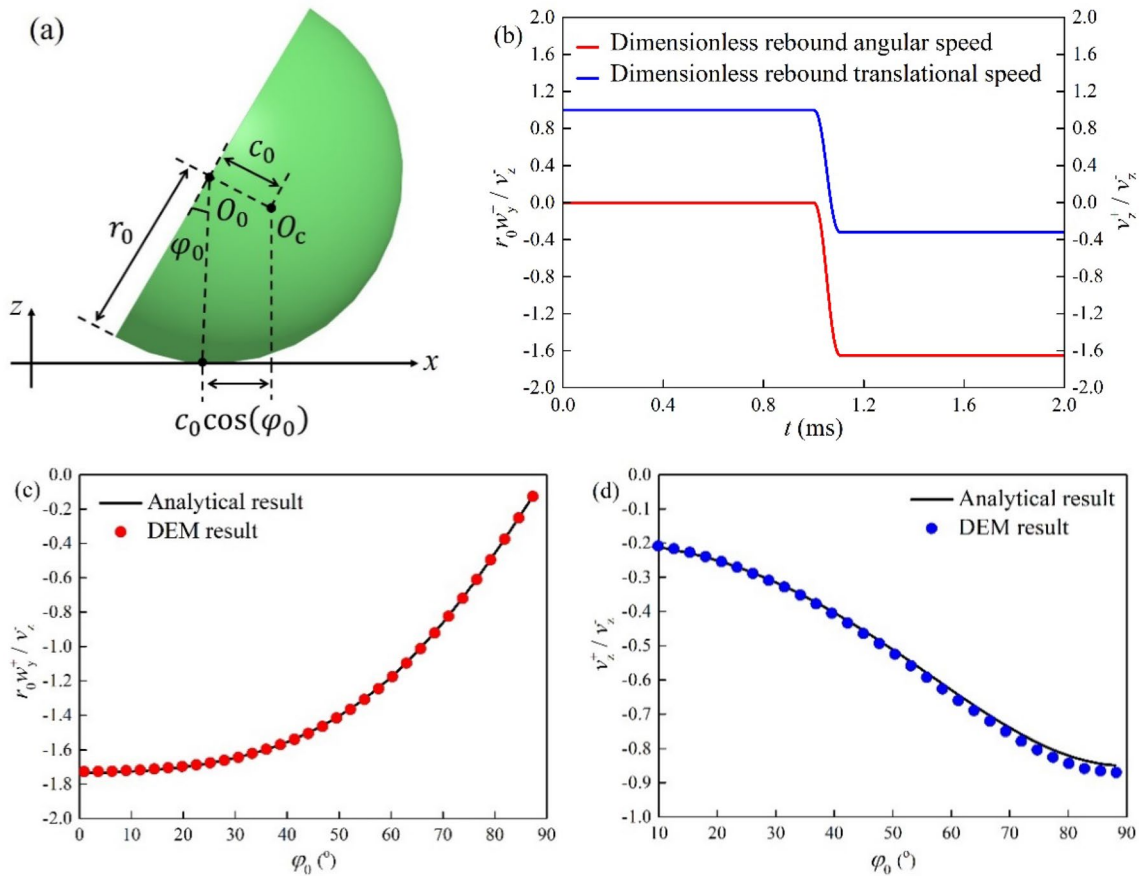
Fig. 8 Comparison between analytical results [49] and DEM results for the hemisphere-wall impact: **a** sketch of the hemisphere-wall impact, **b** time variation of the dimensionless rebound angular speed and translational speed, **c** dimensionless rebound angular speed at different impact angles, $r_0 w_y^+ / v_z^-$, and **d** dimensionless rebound translational speed at different impact angles, v_z^+ / v_z^-

Table 1 Nonlinear contact force model of poly-superquadric elements

Forces and Torques	Symbols	Equations
Normal elastic force	$\boldsymbol{F}_{n,ij}^e$	$4/3 E^* \sqrt{R^*} \delta_n^{3/2}$
Normal damping force	$\boldsymbol{F}_{n,ij}^d$	$C_n \sqrt{8 m^* E^* \sqrt{R^* \delta_n}} \cdot \boldsymbol{v}_{n,ij}$
Tangential elastic force	$\boldsymbol{F}_{t,ij}^e$	$\mu_s \left| \boldsymbol{F}_{n,ij}^e \right| \left(1 - \left(1 - \min \left(\delta_t, \delta_{t,\max} \right) / \delta_{t,\max} \right)^{3/2} \right) \bar{\boldsymbol{t}}$
Tangential damping force	$\boldsymbol{F}_{t,ij}^d$	$C_t \left(6 \mu_s m^* \left| \boldsymbol{F}_{n,ij}^e \right| \sqrt{1 - \min \left(\delta_t, \delta_{t,\max} \right)} / \delta_{t,\max} \right)^{1/2} \boldsymbol{v}_{t,ij}$
Coulomb friction force	$\boldsymbol{F}_{t,ij}^{\max}$	$\mu_s \left| \boldsymbol{F}_{n,ij}^e \right| \bar{\boldsymbol{t}}$
Torque by the normal force	$\boldsymbol{M}_{n,ij}$	$R_{ij} \times \left(\boldsymbol{F}_{n,ij}^e + \boldsymbol{F}_{n,ij}^d \right)$
Torque by the tangential force	$\boldsymbol{M}_{t,ij}$	$R_{ij} \times \left(\boldsymbol{F}_{t,ij}^e + \boldsymbol{F}_{t,ij}^d \right)$
Rolling friction torque	$\boldsymbol{M}_{r,ij}$	$\mu_r R_i \left| \boldsymbol{F}_{n,ij} \right| \overline{\boldsymbol{\omega}}_{ij}$

where $E^* = E/2 \left(1 - v^2 \right)$, $R^* = R_i R_j / \left(R_i + R_j \right)$, $m^* = m_i m_j / \left(m_i + m_j \right)$, $\bar{\boldsymbol{\omega}}_{ij} = \boldsymbol{\omega}_{ij} / |\boldsymbol{\omega}_{ij}|$, $\bar{\boldsymbol{t}} = \boldsymbol{\delta}_t / |\boldsymbol{\delta}_t|$, $\delta_{t,\max} = \mu_s (2 - v)/2(1 - v)\delta_n$. Note that $\boldsymbol{F}_{t,ij}$ should be replaced by $\boldsymbol{F}_{t,ij}^{\max}$ when $\delta_t < \delta_{t,\max}$

Table 2 Major computational parameters of single-particle collision

| Definitions	Value	Definitions	Value
Density (kg/m³)	2500	Normal damping coefficient	0.04
Young's modulus (Pa)	1×10^9	Tangential damping coefficient	0.0
Poisson's ratio	0.3	Sliding friction coefficient	0.0

Table 3 Major parameters of DEM simulations

Definition	Value	Definition	Value
Density (kg/m³)	2500	Normal damping coefficient	0.3
Young's modulus (Pa)	5×10^8	Tangential damping coefficient	0.3
Poisson's ratio	0.25	Sliding friction coefficient	0.3

$r_y^+ : r_y^- = 0.4$, $r_z^+ : r_z^- = 0.5$, and $n_1^* = n_2^* = 2$. A cube-like particle constructed by the superquadric model has parameters of $a : b : c = 1 : 1 : 1$ and $n_1 = n_2 = 6$. Differently shaped particles have the same volume, and the diameter of the volume equivalent sphere is 5 mm. The total number

of particles is 6000, and the DEM parameters are listed in Table 3.

The container has parameters of $L_0 = W_0 = 75$ mm, and the height is 180 mm. Initially, the superquadric and poly-superquadric elements have arbitrary positions and orientations and are dropped into the container, as shown in Fig. 9. It is worth noting that the bounding spheres of particles of different shapes are used to determine the initial contact between the elements, thereby generating a granular system with no overlap between the elements. Particles of different shapes have different radii of the bounding spheres, which results in different generation rates of the particles. The color of the particle represents the height of the particle from the bottom. Red means the height of the particles is higher, and blue means the height of the particles is lower. Finally, all particles are motionless and form a stable system.

Furthermore, the flow processes of non-spherical particles within a cuboid hopper are simulated using superquadric and poly-superquadric DEM models. The hopper has parameters of $L_0 = W_0 = 75$ mm, and the orifice has parameters of $L_1 = W_1 = 25$ mm, as shown in Fig. 10. For particles of different shapes, the hopper angle varies from 15° to 75° to investigate the superimposed influence of the
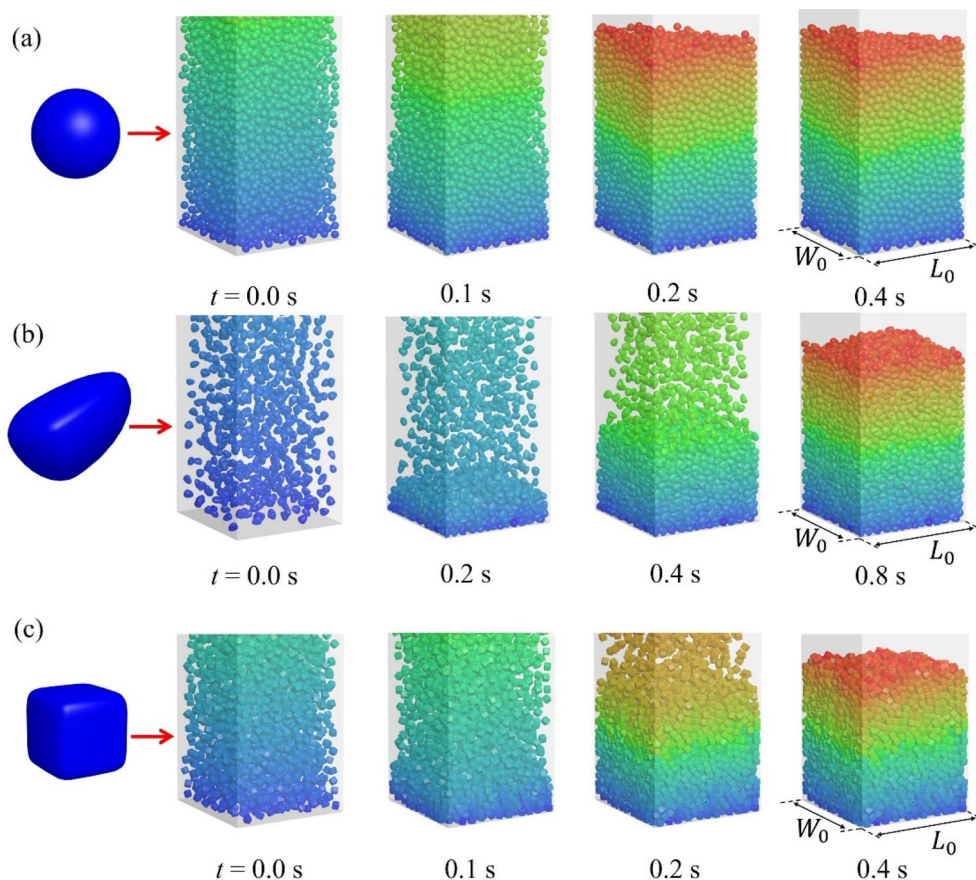
Fig. 9 A stable system composed of particles of different shapes: **a**, **c** superquadric particles and **b** poly-superquadric particles

hopper structure. The formation of a stable particle system is shown in Fig. 9. Then, all the particles are divided into four parts according to height and represented by different colors. Eventually, the orifice is opened when all particles are motionless.

Figure 11 shows snapshots of the discharge processes of particles of different shapes. Here, the base angle is 30°. After the orifice is opened, a V-shaped flow pattern is observed. Meanwhile, the particle shape has a significant influence on the motion behaviors of granular materials. The spherical particles basically have a uniform speed, and the V-shaped pattern is not clearly observed. Moreover, the speed of the cubes near the wall is significantly lower than that of the cubes located at the center of the container. As a result, this flow pattern strengthens for cubes. For the pebble-like particles constructed by poly-superquadric models, the speed of the particles located on the upper layer of the system is uniform, while the velocity distribution of the particles located on the lower layer of the granular bed is not uniform. Moreover, the percentage of the discharged mass of differently shaped particles varies with time as shown in Fig. 12. It is obvious that the particle morphology is a key factor affecting the discharge rate of the granular material. In the following sections, the influence of the hopper angle, surface blockiness, and aspect ratio on the average mass flow rate will be investigated.

Fig. 10 Diagram of the hopper configuration simulated by DEM

Fig. 11 Snapshots of the discharge process of particles of different shapes: **a**, **c** superquadric elements and **b** poly-superquadric elements
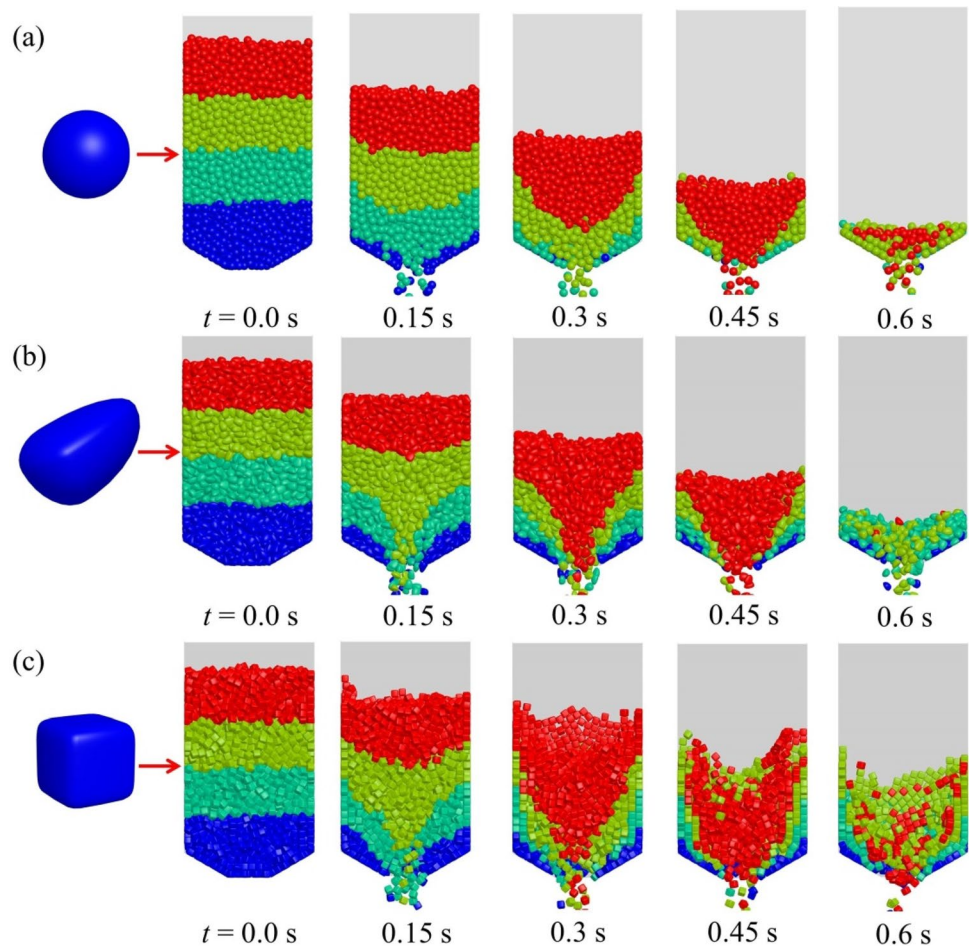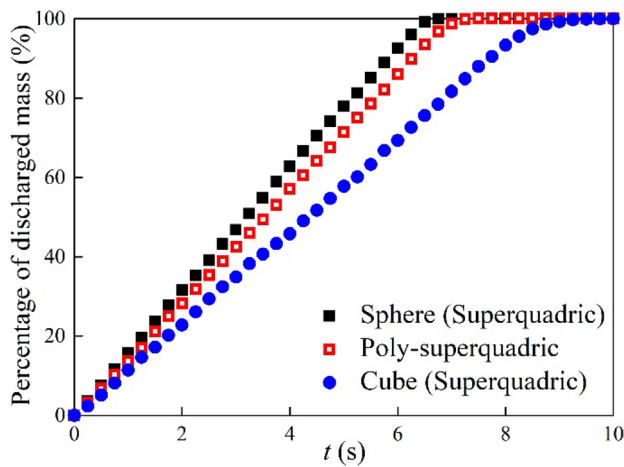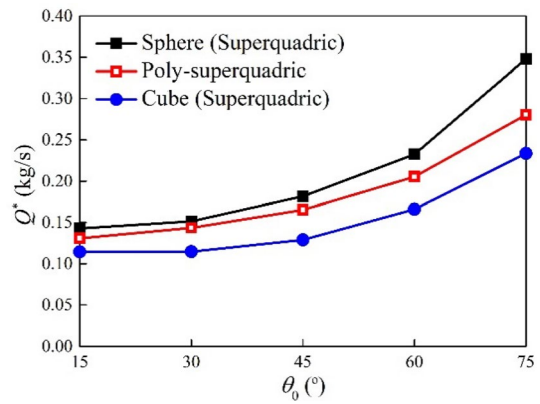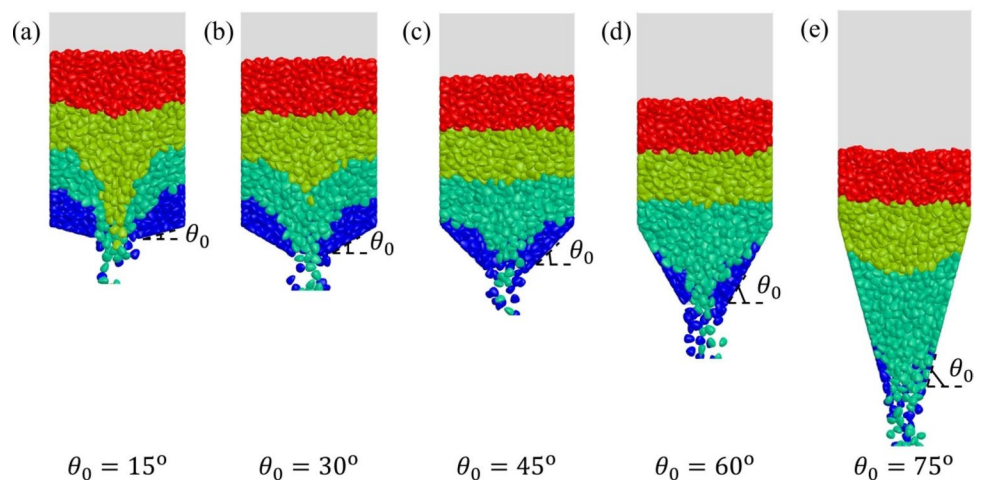
**Fig. 12** Time variation of the percentage of discharged mass for particles of different shapes

Fig. 14 Average mass flow rates for different particle shapes and hopper angles

5.1 Effect of hopper angle on the flow rate

Figure 13 shows the influence of the hopper angle on the discharging process of the poly-superquadric elements. Here, $t = 0.1$ s. As the base angle increases, more particles have a uniform speed and the V-shaped pattern gradually disappears. Moreover, the average mass flow rate (Q^*) of particles of different shapes varies with the hopper angle, as shown in Fig. 14. The average discharge rate of particles increases as the base angle increases. Furthermore, spheres have the fastest flow rate, while the flow rate of pebble-shaped particles constructed by the poly-superquadric model is faster than that of cubes modeled by the superquadric element. It is mainly because the spheres have the smoothest surface, and the surface of the pebble-shaped particles is smoother than that of the cubes. The smooth particle surface facilitates the sliding and rotation of the particles, resulting in a faster flow rate.

5.2 Effect of surface blockiness on the flow rate

Figure 15 shows the influence of blockiness parameters on the superquadric and poly-superquadric elements. Superquadric elements have parameters of $a : b : c = 1 : 1 : 1$, and poly-superquadric elements have parameters of $r_x^+ : r_x^- = 0.7$, $r_y^+ : r_y^- = 0.4$ and $r_z^+ : r_z^- = 0.5$. Particles of different shapes have the same volume, and the equivalent diameter is 5 mm. Figure 16 shows the variation of the average flow rate (Q^*) of superquadric and poly-superquadric particles with blockiness parameters. The flow rate of the non-spherical granular materials decreases with the increase in the blockiness parameter. Meanwhile, superquadric particles have a faster flow rate than poly-superquadric particles. It is mainly because increasing the blockiness parameters may result in close contact between particles and a more ordered packing structure [50]. However, the denser contact mode is not conducive to the sliding and rotation of the

Fig. 13 Snapshots of the discharging process of poly-superquadric elements for different hopper angles

| (a) | (b) | (c) | (d) | (e) |

$\theta_0 = 15°$　　　$\theta_0 = 30°$　　　$\theta_0 = 45°$　　　$\theta_0 = 60°$　　　$\theta_0 = 75°$

Fig. 15 The influence of blockiness parameters on the particle shapes

(a) Superquadric $(n_1 = n_2)$

$n_1 = 2$ 3   4   5   6   7

(b) Poly-superquadric $(n_1^* = n_2^*)$

$n_1^* = 2$ 3   4   5   6   7
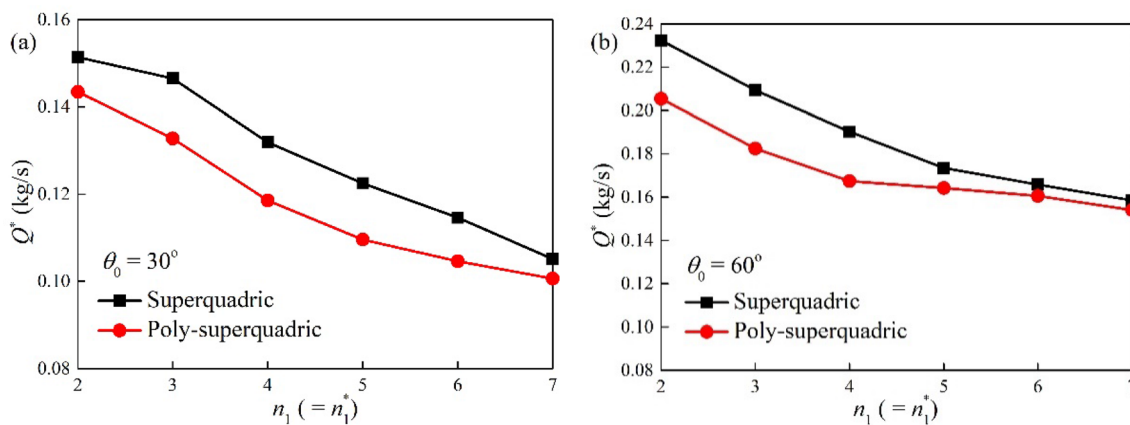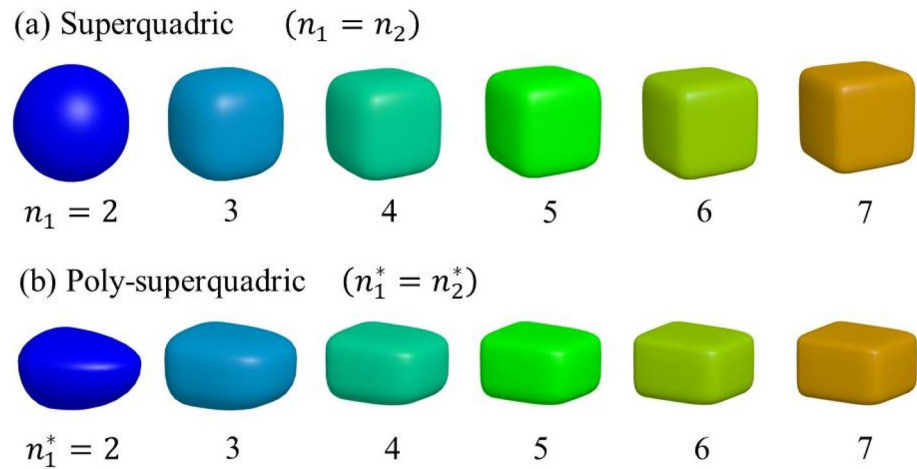
Fig. 16 The influence of blockiness parameters on the average mass flow rates within beds having $\theta = 30°$ (**a**) and $60°$ (**b**)

particles, resulting in a lower flow rate. Moreover, particles modeled by poly-superquadric elements have a greater aspect ratio than those modeled by superquadric elements. Elongated particles are rearranged parallel to the long axis and form an interlocking structure [51], which limits the sliding and rotation between particles and reduces the flow rate of the granular materials.
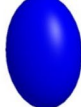
5.3 Effect of aspect ratio on the flow rate

Figure 17 shows particles of different shapes modeled by superquadric and poly-superquadric elements. For particles constructed by superquadric elements, the sphere and cylinder have parameters of $a : b : c = 1 : 1 : 1$, and the ellipsoid has parameters of $a : b : c = 3 : 4 : 5$. For particles constructed by poly-superquadric elements, the hemisphere and semi-cylinder have parameters of $r_x^+ : r_x^- = 3.5$, $r_y^+ : r_y^- = 1$, and $r_z^+ : r_z^- = 1$, and the semi-ellipsoid has parameters of $r_x^+ : r_x^- = 1.5$, $r_y^+ : r_y^- = 1$, and $r_z^+ : r_z^- = 1$. The quarter sphere and the quarter cylinder have the

parameters of $r_x^+ : r_x^- = 3.5, r_y^+ : r_y^- = 3.5$, and $r_z^+ : r_z^- = 1$, and the quarter ellipsoid has parameters of $r_x^+ : r_x^- = 1.5$, $r_y^+ : r_y^- = 2$, and $r_z^+ : r_z^- = 1$. The eighth sphere and eighth cylinder have the parameters of $r_x^+ : r_x^- = 3.5, r_y^+ : r_y^- = 3.5$, and $r_z^+ : r_z^- = 3.5$, and the eighth ellipsoid has parameters of $r_x^+ : r_x^- = 1.5, r_y^+ : r_y^- = 2$, and $r_z^+ : r_z^- = 2.5$. The radius of the volume-equivalent sphere of differently shaped particles is 5 mm.

Figure 18 shows the effect of aspect ratio on the average mass flow rate of particles. The spheres have the fastest flow rate, and the flow rate of the ellipsoids is faster than that of the cylinders. Meanwhile, the flow rate of particles represented by superquadric elements is faster than that of approximately half, one-quarter, and one-eighth particles represented by poly-superquadric elements. Moreover, the approximately one-quarter particles have the lowest flow rate. This is mainly because differently shaped particles have the same volume, which results in the one-quarter particles having the longest length in the z-axis direction. The relative movement between elongated particles is restricted by

Fig. 17 Superquadric and poly-superquadric particles with different aspect ratios

Particle type	Superquadric	Poly-superquadric		
	(a) Entire	(b) Approximate half	(c) Approximate quarter	(d) Approximate one-eighth
Sphere $n_1 = n_2 = 2$ $(n_1^* = n_2^* = 2)$				
Cylinder $n_1 = 6, n_2 = 2$ $(n_1^* = 6, n_2^* = 2)$				
Ellipsoid $n_1 = n_2 = 2$ $(n_1^* = n_2^* = 2)$				
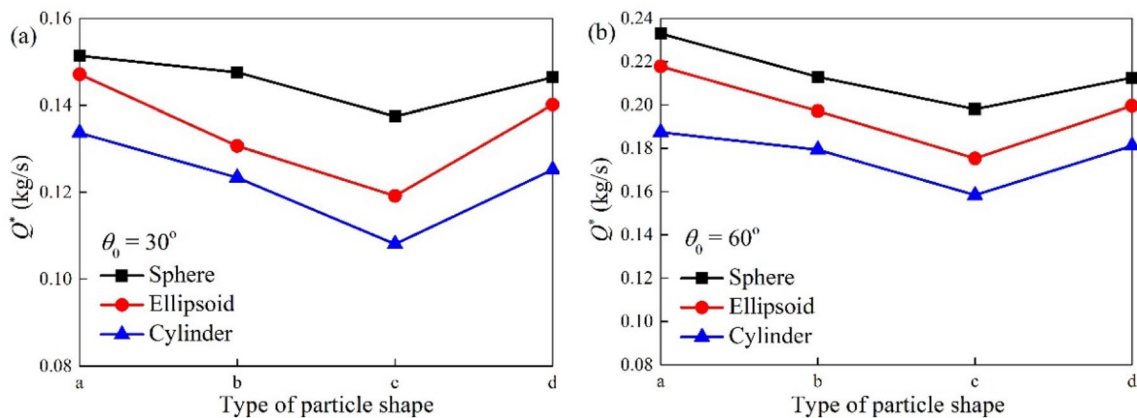
Fig. 18 Average mass flow rates for differently shaped particles within beds having $\theta = 30°$ (**a**) and $60°$ (**b**)

local clusters and interlocking structures, which reduces the flowability of the non-spherical granular materials.

6 Conclusions

In this work, a poly-superquadric method for non-spherical elements has been developed. This model combines eight superquadric equations and eight shape parameters are used to describe the convex and geometrically asymmetric particle shapes. The verification tests consist of a plane impacted by a hemisphere, the packing and discharging process within a cuboid hopper. The DEM results are compared with the theoretical results, which verifies the applicability of poly-superquadric models for the non-spherical granular systems. Subsequently, the effects of the particle shape on the flow rate of non-spherical granular materials are studied. The results show that the spheres have the fastest flow rate, and the flow rate of the pebble-shaped

particles constructed by the poly-superquadric elements is faster than that of the cube-like particles. Moreover, the flow rate of superquadric and poly-superquadric elements decreases as the blockiness parameter increases. In addition, poly-superquadric elements have higher aspect ratios and geometric asymmetry than superquadric elements. These particles tend to form local interlocking and cluster structures, thereby reducing the flow rate of the non-spherical granular materials.

Declarations

Conflict of interest The authors declare that they have no conflict of interest.

References

1. Cundall PA, Strack ODL (1979) A discrete numerical mode for granular assemblies. Géotechnique 29(1):47–65. https://doi.org/10.1680/geot.1979.29.1.47

2. Sinnott MD, Cleary PW (2015) The effect of particle shape on mixing in a high shear mixer. Comput Particle Mech 3(4):477–504. https://doi.org/10.1007/s40571-015-0065-4

3. Xu W, Zhang Y, Jiang J, Liu Z, Jiao Y (2021) Thermal conductivity and elastic modulus of 3D porous/fractured media considering percolation. Int J Eng Sci 161:103456. https://doi.org/10.1016/j.ijengsci.2021.103456

4. Ji S (2013) Probability analysis of contact forces in quasi-solid-liquid phase transition of granular shear flow. Sci China Phys Mech Astron 56(2):395–403. https://doi.org/10.1007/s11433-012-4979-z

5. Xue J, Schiano S, Zhong W, Chen L, Wu C-Y (2019) Determination of the flow/no-flow transition from a flat bottom hopper. Powder Technol 358:55–61. https://doi.org/10.1016/j.powtec.2018.08.063

6. Li Y, Gui N, Yang X, Tu J, Jiang S (2016) Effect of friction on pebble flow pattern in pebble bed reactor. Ann Nucl Energy 94:32–43. https://doi.org/10.1016/j.anucene.2016.02.022

7. Boton M, Azéma E, Estrada N, Radjaï F, Lizcano A (2013) Quasi-static rheology and microstructural description of sheared granular materials composed of platy particles. Phys Rev E 87:032206. https://doi.org/10.1103/PhysRevE.87.032206

8. Höhner D, Wirtz S, Scherer V (2012) A numerical study on the influence of particle shape on hopper discharge within the polyhedral and multi-sphere discrete element method. Powder Technol 226(8):16–28

9. Lu G, Third JR, Müller CR (2015) Discrete element models for non-spherical particle systems: from theoretical developments to applications. Chem Eng Sci 127:425–465. https://doi.org/10.1016/j.ces.2014.11.050

10. Zhong W, Yu A, Liu X, Tong Z, Zhang H (2016) DEM/CFD-DEM Modelling Of Non-Spherical Particulate Systems: Theoretical Developments And Applications. Powder Technol 302:108–152. https://doi.org/10.1016/j.powtec.2016.07.010

11. Kafashan J, Wiącek J, Abd Rahman N, Gan J (2019) Two-dimensional particle shapes modelling for DEM simulations in engineering: a review. Granul Matter 21:80. https://doi.org/10.1007/s10035-019-0935-1

12. Liu L, Ji S (2020) A new contact detection method for arbitrary dilated polyhedra with potential function in discrete element method. Int J Numer Methods Eng. https://doi.org/10.1002/nme.6522

13. Cleary PW (2019) Effect of rock shape representation in DEM on flow and energy utilisation in a pilot SAG mill. Comput Particle Mech 6(3):461–477. https://doi.org/10.1007/s40571-019-00226-3

14. Gong Z, Wu Y, Zhu Z, Wang Y, Liu Z, Xu W (2020) DEM and dual-probability-Brownian motion scheme for thermal conductivity of multiphase granular materials with densely packed non-spherical particles and soft interphase networks. Comput Methods Appl Mech Eng 372:113372. https://doi.org/10.1016/j.cma.2020.113372

15. He SY, Gan JQ, Pinson D, Yu AB, Zhou ZY (2019) Flow regimes of cohesionless ellipsoidal particles in a rotating drum. Powder Technol 354:174–187. https://doi.org/10.1016/j.powtec.2019.05.083

16. Tangri H, Guo Y, Curtis JS (2019) Hopper discharge of elongated particles of varying aspect ratio: experiments and DEM simulations. Chem Eng Sci X 4:100040. https://doi.org/10.1016/j.cesx.2019.100040

17. Govender N, Wilke DN, Pizette P, Abriak N-E (2018) A study of shape non-uniformity and poly-dispersity in hopper discharge of spherical and polyhedral particle systems using the Blaze-DEM GPU code. Appl Math Comput 319:318–336. https://doi.org/10.1016/j.amc.2017.03.037

18. Höhner D, Wirtz S, Scherer V (2013) Experimental and numerical investigation on the influence of particle shape and shape approximation on hopper discharge using the discrete element method. Powder Technol 235:614–627. https://doi.org/10.1016/j.powtec.2012.11.004

19. Zhao Y, Chew JW (2020) Discrete element method study on hopper discharge behaviors of binary mixtures of nonspherical particles. AIChE J 66(8):e16254. https://doi.org/10.1002/aic.16254

20. Li C, Peng Y, Zhang P, Zhao C (2019) The contact detection for heart-shaped particles. Powder Technol 346:85–96. https://doi.org/10.1016/j.powtec.2019.01.079

21. Garboczi EJ, Bullard JW (2017) 3D analytical mathematical models of random star-shape particles via a combination of X-ray computed microtomography and spherical harmonic analysis. Adv Powder Technol 28(2):325–339. https://doi.org/10.1016/j.apt.2016.10.014

22. Kawamoto R, Andò E, Viggiani G, Andrade JE (2016) Level set discrete element method for three-dimensional computations with triaxial case study. J Mech Phys Solids 91:1–13. https://doi.org/10.1016/j.jmps.2016.02.021

23. Boon CW, Houlsby GT, Utili S (2013) A new contact detection algorithm for three-dimensional non-spherical particles. Powder Technol 248:94–102. https://doi.org/10.1016/j.powtec.2012.12.040

24. Mollon G, Zhao J (2014) 3D generation of realistic granular samples based on random fields theory and Fourier shape descriptors. Comput Methods Appl Mech Eng 279:46–65. https://doi.org/10.1016/j.cma.2014.06.022

25. Feng YT, Han K, Owen DRJ (2012) Energy-conserving contact interaction models for arbitrarily shaped discrete elements. Comput Methods Appl Mech Eng 205(1):169–177

26. Feng YT (2021) An energy-conserving contact theory for discrete element modelling of arbitrarily shaped particles: Basic framework and general contact model. Comput Methods Appl Mech Eng. https://doi.org/10.1016/j.cma.2020.113454

27. Meng L, Wang C, Yao X (2018) Non-convex shape effects on the dense random packing properties of assembled rods. Phys A 490:212–221. https://doi.org/10.1016/j.physa.2017.08.026

28. Zhao B, An X, Zhao H, Shen L, Sun X, Zhou Z (2019) DEM simulation of the local ordering of tetrahedral granular matter. Soft Matter 15(10):2260–2268. https://doi.org/10.1039/c8sm02166j

29. Yu F, Zhang S, Zhou G, Zhang Y, Ge W (2018) Geometrically exact discrete-element-method (DEM) simulation on the flow and mixing of sphero-cylinders in horizontal drums. Powder Technol 336:415–425. https://doi.org/10.1016/j.powtec.2018.05.040

30. Rakotonirina AD, Delenne J-Y, Radjai F, Wachs A (2019) Grains3D, a flexible DEM approach for particles of arbitrary convex shape—part III: extension to non-convex particles modelled as glued convex particles. Comput Particle Mech 6(1):55–84. https://doi.org/10.1007/s40571-018-0198-3

31. Peters John F (2009) A poly-ellipsoid particle for non-spherical discrete element method. Eng Comput 26(6):645–657. https://doi.org/10.1108/02644400910975441

32. Zhang B, Regueiro R, Druckrey A, Alshibli K (2018) Construction of poly-ellipsoidal grain shapes from SMT imaging on sand, and the development of a new DEM contact detection algorithm. Eng Comput 35(2):733–771. https://doi.org/10.1108/ec-01-2017-0026

33. Liu Z, Zhao Y (2020) Multi-super-ellipsoid model for non-spherical particles in DEM simulation. Powder Technol 361:190–202. https://doi.org/10.1016/j.powtec.2019.09.042

34. Zhao S, Zhao J (2019) A poly-superellipsoid-based approach on particle morphology for DEM modeling of granular media. Int J Numer Anal Meth Geomech 43(13):2147–2169. https://doi.org/10.1002/nag.2951

35. Barrr AH (1981) Superquadrics and angle-preserving transformations. IEEE Comput Gr Appl 1(1):11–23. https://doi.org/10.1109/MCG.1981.1673799

36. Zhao Y, Xu L, Umbanhowar PB, Lueptow RM (2019) Discrete element simulation of cylindrical particles using super-ellipsoids. Particuology 46:55–66. https://doi.org/10.1016/j.partic.2018.04.007

37. Chen H, Zhao S, Zhou X (2020) DEM investigation of angle of repose for super-ellipsoidal particles. Particuology 50:53–66. https://doi.org/10.1016/j.partic.2019.05.005

38. Eberly D (2002) Dynamic collision detection using oriented bounding boxes. Geometric tools

39. Wellmann C, Lillie C, Wriggers P (2008) A contact detection algorithm for superellipsoids based on the common-normal concept. Eng Comput 25(5):432–442. https://doi.org/10.1108/02644400810881374

40. Houlsby GT (2009) Potential particles: a method for modelling non-circular particles in DEM. Comput Geotech 36(6):953–959. https://doi.org/10.1016/j.compgeo.2009.03.001

41. Podlozhnyuk A, Pirker S, Kloss C (2016) Efficient implementation of superquadric particles in discrete element method within an open-source framework. Comput Particle Mech 4(1):101–118. https://doi.org/10.1007/s40571-016-0131-6

42. Soltanbeigi B, Podlozhnyuk A, Papanicolopulos S-A, Kloss C, Pirker S, Ooi JY (2018) DEM study of mechanical characteristics of multi-spherical and superquadric particles at micro and macro scales. Powder Technol 329:288–303. https://doi.org/10.1016/j.powtec.2018.01.082

43. Zhu HP, Zhou ZY, Yang RY, Yu AB (2007) Discrete particle simulation of particulate systems: theoretical developments. Chem Eng Sci 62(13):3378–3396. https://doi.org/10.1016/j.ces.2006.12.089

44. Zhou ZY, Zou RP, Pinson D, Yu A-B (2011) Dynamic simulation of the packing of ellipsoidal particles. Ind Eng Chem Res 50(16):9787–9798. https://doi.org/10.1021/ie200862n

45. Dong K, Wang C, Yu A (2015) A novel method based on orientation discretization for discrete element modeling of non-spherical particles. Chem Eng Sci 126:500–516. https://doi.org/10.1016/j.ces.2014.12.059

46. Fritzer HP (2001) Molecular symmetry with quaternions. Spectrochim Acta Part A 57(10):1919–1930. https://doi.org/10.1016/S1386-1425(01)00477-2

47. Kosenko II (1998) Integration of the equations of a rotational motion of a rigid body in quaternion algebra: The Euler case. J Appl Math Mech 62(2):193–200. https://doi.org/10.1016/S0021-8928(98)00025-2

48. Tfm III, Eleftheriou M, Pattnaik P, Ndirango A, Newns D, Martyna GJ (2002) Symplectic quaternion scheme for biophysical molecular dynamics. J Chem Phys 116(20):8649–8659. https://doi.org/10.1063/1.1473654

49. Kodam M, Bharadwaj R, Curtis J, Hancock B, Wassgren C (2010) Cylindrical object contact detection for use in discrete element method simulations, Part II—Experimental validation. Chem Eng Sci 65(22):5863–5871. https://doi.org/10.1016/j.ces.2010.08.007

50. Wang S, Fan Y, Ji S (2018) Interaction between super-quadric particles and triangular elements and its application to hopper discharge. Powder Technol 339:534–549. https://doi.org/10.1016/j.powtec.2018.08.026

51. Langston PA, Al-Awamleh MA, Fraige FY, Asmar BN (2004) Distinct element modelling of non-spherical frictionless particle flow. Chem Eng Sci 59(2):425–435. https://doi.org/10.1016/j.ces.2003.10.008